

Radiation-driven outflows in AGNs: Revisiting feedback effects of scattered and reprocessed photons

Amin Mosallanezhad^{1,2*}, Feng Yuan^{2,3†}, Jeremiah P. Ostriker⁴,
Fatemeh Zahra Zeraatgari⁵, and De-Fu Bu²

¹ Key Laboratory for Research in Galaxies and Cosmology, Department of Astronomy, University of Science and Technology of China, Hefei, Anhui 230036, PR China

² Key Laboratory for Research in Galaxies and Cosmology, Shanghai Astronomical Observatory, Chinese Academy of Sciences, 80 Nandan Road, Shanghai 200030, PR China

³ School of Astronomy and Space Sciences, University of Chinese Academy of Sciences, No. 19A Yuquan Road, Beijing 100049, China

⁴ Department of Astronomy, Columbia University, 550 W, 120th Street, New York, NY10027, USA

⁵ School of Mathematics and Statistics, Xian Jiaotong University, Xian 710049, China

3 January 2022

ABSTRACT

We perform two-dimensional hydrodynamical simulations of slowly rotating accretion flows in the region of $0.01 - 7\text{ pc}$ around a supermassive black holes with $M_{\text{BH}} = 10^8 M_{\odot}$. The accretion flow is irradiated by the photons from the central active galactic nucleus (AGN). In addition to the direct radiation from the AGN, we have also included the “re-radiation”, i.e., the locally produced radiation by Thomson scattering, line and bremsstrahlung radiation. Compare to our previous work, we have improved the calculation of radiation force due to the Thomson scattering of X-ray photons from the central AGN. We find that this improvement can significantly increase the mass flux and velocity of outflow. We have compared the properties of outflow — including mass outflow rate, velocity, and kinetic luminosity of outflow — in our simulation with the observed properties of outflow in AGNs and found that they are in good consistency. This implies that the combination of line and re-radiation forces is the possible origin of observed outflow in luminous AGNs.

Key words:

accretion, accretion discs – hydrodynamics – methods: numerical – galaxies: active – galaxies: nuclei.

1 INTRODUCTION

It is believed that AGN feedback plays an important role in the formation and evolution of their host galaxies (Fabian 2012; Kormendy & Ho 2013). The most remarkable observational evidence is the strong correlation between the mass of the supermassive black holes (SMBHs) and the properties of the host galactic bulge, such as luminosity (Kormendy & Richstone 1995), velocity dispersion (Gebhardt et al. 2000; Ferrarese & Merritt 2000; Tremaine et al. 2002; Gültekin et al. 2009; Graham et al. 2011), and stellar mass (Magorrian et al. 1998; Marconi & Hunt 2003; Häring & Rix 2004). The importance of AGN feedback has also been confirmed by many theoretical studies especially numerical simulations, from cosmological to galactic scales (see e.g., Ostriker et al.

2010; Gan et al. 2014, 2019; Yuan et al. 2018; Yoon et al. 2018; Li et al. 2018).

The three kinds of outputs from AGNs are radiation, jet, and wind. Especially, it has been found that wind plays an important role in AGN feedback (e.g., Ostriker et al. 2010). When the accretion rate of AGN is low, the accretion and feedback are in the hot mode. In this case, wind is driven by the combination of thermal and magnetic forces and the mass flux of wind can be much larger than the net accretion rate (e.g., Blandford & Begelman 1999; Yuan et al. 2012a,b; Narayan et al. 2012; Li et al. 2013; Yuan et al. 2015; Bu et al. 2016; Mosallanezhad et al. 2016). This kind of “hot” wind has been confirmed by observations (e.g., Wang et al. 2013; Tombesi et al. 2014; Homan et al. 2016; Cheung et al. 2016; Ma et al. 2019) and found to play an important role in AGN feedback (e.g., Weinberger et al. 2017a; Yuan et al. 2018).

In the case of the cold accretion mode, a wind can be driven by the AGN radiation and magnetic field of the ac-

* E-mail: mosallanezhad@ustc.edu.cn

† E-mail: fyuan@shao.ac.cn

cretion disc. In this paper we will focus on the radiation mechanism. If the gas is fully ionized, radiation exerts a force on the gas through Thomson scattering. In the case of partially ionized gas, the cross section of interaction between UV photons and the gas can be several thousands of times larger than that of Thomson scattering (e.g., Proga et al. 2000; Proga 2007a; Proga et al. 2008; Korusawa & Proga 2008, 2009). Therefore, line force can be significantly stronger than the radiation force due to Thomson scattering.

Following this line, Korusawa & Proga (2009) (hereafter KP09) have presented hydrodynamical simulations to investigate the interaction between radiation and slowly rotating gas at parsec (pc) scale. Their computational domain covers a range from $\sim 10^{-2}$ to 7 pc. They assumed that when gas falls into the region $< 10^{-2}$ pc, an accretion disc will be formed. A spherical hot corona is assumed to be present above the disc and is responsible for the X-ray radiation of the AGN. The total accretion luminosity is self-consistently determined by calculating mass accretion rate at the inner boundary of the computational domain and by assuming a canonical radiative efficiency of the standard thin disc. The X-rays radiation will ionize the accretion flow at pc scale, and will also produce a radiation pressure through Thomson scattering. For the optical/UV photons from the AGN, in addition to the radiation force due to Thomson scattering, they will also interact with partially ionized gas and exert a much stronger line force.

In KP09 and other similar previous works, the authors only considered the radiation directly coming from the central AGNs. In reality, the locally generated photons through scattering, bremsstrahlung and line radiation in the gas far away from the AGN can also play an important role. The radiation force due to the locally generated photons is called “re-radiation” force. Liu et al. (2013) investigated the effects of re-radiation force on the dynamics of the flow at parsec scale and found that the accretion flow becomes thicker due to the additional vertical component of the re-radiation force and the outflow becomes stronger consequently.

For calculating the radiation force due to the Thomson scattering of X-ray photons from the central AGN, KP09 made use of $F = F_X \kappa_{es} / c$ (F_X is the X-ray flux, κ_{es} is Thomson scattering opacity, c is the speed of light). However in Liu et al. (2013), the author used another formula to calculate this force. The formula adopted in Liu et al. (2013) is that $F = \dot{E} / (\rho c)$, with \dot{E} being the Compton heating rate, and ρ is the gas density. We think the formula used in Liu et al. (2013) does not correctly represent the force due to the Thomson scattering. For instance, this force will be incorrectly equal to zero if the “Compton temperature” is equal to the gas temperature. Therefore, in the present paper, we use the same formula adopted in KP09 to calculate the radiation force due to the Thomson scattering of X-ray photons from the central AGN. We will make this correction and investigate how the result will be changed compared to Liu et al. (2013).

There is some observational evidence for AGNs with sub-Eddington luminosity. For instance, Kollmeier et al. 2006 in a study on 407 AGNs in the redshift range $Z \sim 0.3 - 4$ has found that the most of the AGNs in the sample are sub-Eddington. Indeed, they described the luminosity distribution of the estimated Eddington ratios by log-normal which the maximum value is $L_{\text{bol}} / L_{\text{Edd}} \approx 1/4$ (L_{bol}

and L_{Edd} being bolometric and Eddington luminosity, respectively. Steinhardt & Elvis 2010 used a large sample of 62185 quasars from SDSS. They also obtained same results. In fact, the broad mass distribution of the fuelling gas of the galactic scale can provide enough gas to fuel the AGNs to have super-Eddington luminosities. Moreover, based on slim accretion disk model, the rotating accretion disk can have super-Eddington luminosity (Abramowicz et al. 1988; Ohsuga et al. 2005; Yang et al. 2014). Therefore, the sub-Eddington accretion of the AGNs is a problem which should be solved.

One proposed solution for the problem of sub-Eddington puzzle is AGN radiative feedback. Nevertheless, the inefficiency of the radiative feedback for innermost region of the slim disk is shown by numerical simulation done by Ohsuga et al. 2005. They showed, by considering radiative transfer, the central region of the black hole accretion flow can radiate well above the Eddington luminosity. On parsec scale, KP09 showed that the line force can drive strong wind, however the radiative feedback could not solve the sub-Eddington puzzle in their numerical results. In this paper, we try to solve this puzzle by adding the re-radiation force.

The structure of the paper is as follows. We describe our method, model assumptions, and modifications to the Liu et al. 2013 work in sections 2 and 3. The results of our simulations will be given in Section 4. In section 5, we will discuss and summarize the main results.

2 NUMERICAL METHOD

We perform axisymmetric two-dimensional hydrodynamic (HD) simulations, by using grid-based multidimensional code ZEUS-MP (Hayes et al. 2006), which is the massive parallel MPI-implemented version of the ZEUS-3D code (Hardee & Clarke 1992; Clarke 1996). Our basic physical setup is mostly the same as one used in Liu et al. 2013 (see also Korusawa & Proga 2008, 2009). We outline our numerical method and all differences from Liu et al. 2013 below.

2.1 Basic Equations

We consider a SMBH located at the origin of the polar coordinate system which is surrounded by an accretion flow. To compute the evolution and the structure of the accretion flow irradiated by the strong radiation from AGN, we solve the following set of equations,

$$\frac{d\rho}{dt} + \rho \nabla \cdot \mathbf{v} = 0, \quad (1)$$

$$\rho \frac{d\mathbf{v}}{dt} = -\nabla p - \rho \nabla \psi + \rho \mathbf{F}_{\text{rad}}, \quad (2)$$

$$\rho \frac{d(e/\rho)}{dt} = -p \nabla \cdot \mathbf{v} + \rho \mathcal{L}, \quad (3)$$

where ρ , \mathbf{v} , p , e , and ψ are mass density, velocity, gas pressure, internal energy density, and gravitational potential, respectively. We employ the pseudo-Newtonian potential, $\psi = -GM/(r-r_s)$ (Paczynsky & Wiita 1980), where M and

G are the centre BH mass and the gravitational constant, respectively, and $r_s \equiv 2GM/c^2$. The Lagrangian/comoving derivative is given by $d/dt \equiv \partial/\partial t + \mathbf{v} \cdot \nabla$. We adopt the adiabatic equation of state in the form of $p = (\gamma - 1)e$, where γ is the adiabatic index and is set to be $\gamma = 5/3$. Here, \mathbf{F}_{rad} is the total radiation force per unit mass, and \mathcal{L} in the energy equation, Equation (3), denotes the net cooling rate. Both radiation force and net cooling rate will be described in more details in the following section.

2.2 Model Setup

To solve equations (1)–(3), we use spherical polar coordinates (r, θ, ϕ) , where r is the distance from the origin of the coordinates, θ is the polar angle and ϕ is the azimuthal angle. We set the two-dimensional computational domain of $r_{\min} \leq r \leq r_{\max}$ and $\epsilon \leq \theta \leq \pi/2$, where ϵ is set to be a small value to avoid the numerical singularity near the polar axis. For all the runs presented here, we set $r_{\min} = 500r_*$, and $r_{\max} = 2.5 \times 10^5 r_*$, where $r_* = 3r_s$ is the innermost stable circular orbit (ISCO) of a Schwarzschild BH. We divide the $r - \theta$ plane into zones as follows: in r direction, we have 144 zones with the zone size ratio $dr_{i+1}/dr_i = 1.04$, which ensures good resolution near the inner region of our computational domain. In the θ direction, we have 64 zones with $d\theta_{j+1}/d\theta_j = 1.0$ (i.e., equally spaced grids).

For initial conditions, we adopt the uniform density and gas temperature everywhere in the computational domain, i.e., $\rho(r, \theta) = \rho_0$ and $T(r, \theta) = T_0$. We set the initial radial and latitudinal components of the velocity to be zero, $v_r(r, \theta) = v_\theta(r, \theta) = 0$, and the angular velocity of the gas is assigned to have the following specific angular momentum distribution,

$$v_\phi(r, \theta) = \begin{cases} 0 & \text{for } r < 10^5 r_* \\ l/(r \sin \theta) & \text{for } r \geq 10^5 r_*. \end{cases} \quad (4)$$

where, l is the latitude-dependent specific angular momentum given as,

$$l(\theta) = l_0(1 - |\cos \theta|), \quad l_0 = \sqrt{GM_{\text{BH}} r_{\text{cir}}}. \quad (5)$$

Here, r_{cir} is the “circularization radius” on the equatorial plane. We set $r_{\text{cir}} = 300r_*$, which is much smaller than the radial inner boundary of our simulation domain. We consider the relatively small value of r_{cir} to prevent the formation of a rotationally supported torus in our computational domain and the complexities associated with it.

The boundary conditions are set as follows. We apply axisymmetric boundary conditions at the rotation axis (i.e., $\theta = 0$) and reflecting boundary conditions at the equatorial plane ($\theta = \pi/2$). At the inner radial boundary, we use outflow boundary conditions (e.g., [Stone & Norman 1992](#)). At the outer radial boundary, if the gas flows in ($v_r(r_{\max}, \theta) < 0$), all HD quantities except the radial component of the velocity, v_r , are set to the initial conditions, i.e., $\rho(r_{\max}, \theta) = \rho_0$, $T(r_{\max}, \theta) = T_0$, $v_\theta(r_{\max}, \theta) = 0$, and $v_\phi(r_{\max}, \theta) = l/(r_{\max} \sin \theta)$. When $v_r(r_{\max}, \theta) > 0$, we use outflow boundary conditions. This approach is adopted to mimic the situation where there is always gas available for accretion and represents steady conditions at the outer radial boundary.

3 RADIATIVE HEATING/COOLING AND RADIATION FORCE

3.1 Modeling of the central AGN

We assume that the accretion flow in the central AGN has two components: a standard thin disc located at the equator ([Shakura & Sunyaev 1973](#)), and a hot corona above the thin disc. We also assume that the innermost edge of the disc is located at r_* and the outer boundary of the disc is much smaller than the inner boundary of the computational domain, i.e., $r_d \ll r_{\min}$. We assume that the disc only emits optical/UV photons (i.e., $L_d = L_{\text{UV}}$), and the hot corona only emits X-ray, $L_* = L_X$. The total luminosity then includes both the luminosity of the disc and the corona, $L_{\text{acc}} = L_d + L_*$. Following KP09, we further assume that the extended disk radiation contributes to the radiation force due to both line force as well as electron scattering. Whereas, the corona radiation contributes to the radiation force only due to the electron scattering (line force contributions of the corona radiation has been ignored). We define the parameter f_* as the ratio of the corona luminosity to the total luminosity, $L_* = f_* L_{\text{acc}}$, and $f_d = 1 - f_*$ as the fraction of the total luminosity in the disc emission. We set $f_* = 0.05$ throughout this paper.

Since the inner boundary of our computational domain is far from the outer edge of the disc, $r_d \ll r_{\min}$, we can safely adopt point-source approximation,

$$\mathcal{F}_*(r) = \frac{L_*}{4\pi r^2} = \frac{f_* L_{\text{acc}}}{4\pi r^2}, \quad (6)$$

$$\mathcal{F}_d(r, \theta) = 2|\cos \theta| \frac{f_d L_{\text{acc}}}{4\pi r^2}. \quad (7)$$

In equation (7), the factor “2” comes from the normalization of the flux. In the present work, we do not consider the UV attenuation due to Thomson scattering, i.e., we assume $\tau_x = \tau_{\text{uv}} = 0$ in the calculations of radiation fluxes from the central engine. This is based on two considerations. The first reason is as stated in detail in KP09 and references therein. The calculation of line force adopted here (and also in other works such as KP09 and [Liu et al. 2013](#)) is taken from a simplified approach proposed in [Stevens & Kallman 1990](#). But this approach is based on the assumption that the radiation is optically thin. So to be consistent, we neglect the optical depth¹. In our parameter regime, optical depth is dominated by scattering. Unlike true absorption, scattering merely re-directs the photons. The scattered X-ray photons must be replenished by photons scattered from other propagation lines. Indeed, with pure scattering there is no attenuation, but only re-direction. This is another reason why we neglect the optical depth.

3.2 Mass accretion rate and accretion luminosity

In our simulation, at each time step, the accretion luminosity will be updated self-consistently based on the mass accretion rate, $\dot{M}_a(t)$, calculated at the inner boundary of

¹ We do include the X-ray optical depth when we calculate the ionization parameter

our computational domain, r_{\min} . The accretion luminosity is then,

$$L_{\text{acc}}(t) = \eta \dot{M}_a(t) c^2, \quad (8)$$

where η is the radiative efficiency and set to be $\eta = 1/12$ in this paper since we assume the disc is described by the standard thin disc model. Following KP09 and Liu et al. 2013, the time averaged mass accretion rate can be expressed as,

$$\dot{M}_a(t) = \frac{\int_{t-\tau-\Delta t}^{t-\tau} \dot{M}(t') dt'}{\int_{t-\tau-\Delta t}^{t-\tau} dt'}, \quad (9)$$

where τ denotes a time lag between the change of the mass accretion rate and the change of the accretion luminosity from the central engine. Since the standard thin disc model is considered here, the lag time can be approximated by accretion time scale as $t_{\text{acc}} \approx r_d/v_r = r_d/(\alpha c_s H/r_d)$. Here, c_s is the isothermal sound speed, H is the half thickness of the disc and α is the viscosity parameter. According to our settings, the lag time will be approximately $\tau \approx 10^9$ seconds². By setting $\Delta t = \tau$ the denominator of the equation (9) becomes τ .

3.3 Radiative cooling/heating

The net cooling rate in the energy equation consists of four heating/cooling terms including Compton heating/cooling, (G_{Comp}), X-ray photoionization heating and recombination cooling, (G_X), cooling via line emission (L_{line}) and bremsstrahlung cooling (L_{brem}). The net cooling rate is as follows (Blondin 1994):

$$\rho \mathcal{L} = n^2 (G_{\text{Comp}} + G_X - L_{\text{line}} - L_{\text{brem}}), \quad (10)$$

where

$$G_{\text{Comp}} = 8.9 \times 10^{-36} \xi (T_X - 4T), \quad (11)$$

$$G_X = 1.5 \times 10^{-21} \xi^{1/4} T^{-1/2} (1 - T/T_X), \quad (12)$$

$$L_{\text{line}} = \left[1.7 \times 10^{-18} \exp(T_l/T) \xi^{-1} T^{-1/2} + 10^{-24} \right] \delta, \quad (13)$$

$$L_{\text{brem}} = 3.3 \times 10^{-27} T^{1/2}, \quad (14)$$

where $n = \rho/(\mu m_p)$ is the number density of the local gas located at the distance r from the AGN, m_p denotes the proton mass, and μ is the mean molecular weight which is set to be 1. In the above equations, $T_X = 8 \times 10^7$ K is the “characteristic temperature” or “Compton” temperature of the X-ray radiation (Sazonov et al. 2004) and T_l parameterizes the line cooling temperature ($T_l = 1.3 \times 10^5$ K). The parameter δ in the line cooling rate is used to control line cooling ($\delta < 1$ represents optically thick cooling and $\delta = 1$ represents optically thin cooling). We set $\delta = 1$. In general, the line cooling dominates over the other cooling processes. According to the Blondin formula, the net cooling rate depends

on the gas temperature, T , density, and the photoionization parameter ξ . The photoionization parameter is expressed as,

$$\xi \equiv \frac{f_* L_{\text{acc}}}{n r^2} e^{-\tau_x}, \quad (15)$$

where,

$$\tau_x = \int_{r_{\min}}^r \rho \kappa_x dr. \quad (16)$$

Here, τ_x is the X-ray scattering optical depth in the radial direction, and $\kappa_x = 0.4 \text{ cm}^2 \text{ g}^{-1}$ is the opacity.

3.4 The radiation force

Both the photons from the central AGN and those locally produced can exert radiation force on gas, so

$$\mathbf{F}_{\text{rad}} = \mathbf{F}_c + \mathbf{F}_{\text{re}}, \quad (17)$$

where \mathbf{F}_c denotes the radiation force due to the central AGN and \mathbf{F}_{re} denotes the re-radiation force due to the locally produced photons.

Let us first calculate \mathbf{F}_c . First, since the gas is not fully ionized, there should be a force corresponding to photoionization heating-recombination cooling (e.g., Liu et al. 2013 and references therein):

$$\dot{E}_X/\rho c = n^2 G_X/\rho c. \quad (18)$$

For the optical/UV radiation from the AGN, there are two components of force, which are due to Thomson scattering and line force, respectively,

$$\mathbf{F}_{c,o} = 2 \frac{\kappa_{es}}{c} \frac{L_{\text{acc}}}{4\pi r^2} f_d [1 + \mathcal{M}(t)] |\cos \theta| \hat{\mathbf{r}}. \quad (19)$$

In the above equation, \mathcal{M} represents the force multiplier (Castor et al. 1975) that is to parameterize how much spectral lines increase the scattering coefficient (see Proga et al. 2000 for more details).

For the X-ray radiation from the AGN, we only consider the force due to Thomson scattering:

$$\mathbf{F}_{c,X} = \frac{\kappa_{es}}{c} \frac{L_{\text{acc}}}{4\pi r^2} f_* \hat{\mathbf{r}}. \quad (20)$$

The total force due to radiation from the central AGN is,

$$\mathbf{F}_c = \frac{n^2 G_X}{\rho c} + \mathbf{F}_{c,o} + \mathbf{F}_{c,X}. \quad (21)$$

Compare this equation with equation (13) in Liu et al. 2013, the difference is that we now correctly include the force due to Thomson scattering of X-ray photons from the central AGN. We expect that the wind will become stronger as a consequence.

The calculation of the re-radiation force (the second term in equation (17)) is exactly the same as that in Liu et al. 2013. For convenience, we briefly introduce as follows. The plane-parallel approximation is adopted in our simple radiative transfer calculation. In this case, the re-radiation force will be in z-direction. By applying the Gauss theorem, the vertical radiative force is described by,

$$\mathbf{F}_{\text{re}} = \frac{\kappa_{es}}{c} \int_0^z (S_c + n^2 L_{\text{brem}} + n^2 L_{\text{line}}) dz \quad (22)$$

² It should be noted here that the results are not so sensitive to the value of τ .

where

$$S_c = \rho \kappa_{\text{es}} \cdot \frac{L_{\text{acc}}}{4\pi r^2} [f_* + 2 f_d |\cos \theta|] \quad (23)$$

is the source term due to the first-order scattered photons of the radiation from the central AGN.

4 RESULTS

We have performed 10 simulations with different values of ρ_0 and T_0 at the outer boundary to explore the effects of these parameters (see columns 3 and 4 of Table 1). The model parameters and some basic results are summarized in Table 1. In models 1, 2, 3 and 4, the calculation of radiation force due to central AGN X-ray photons is the same as that in Liu et al. 2013. In models 5-10, we use the new formula to calculate the radiation force due to central AGN X-ray photons (see Section 3.4). To quantitatively study the flows, we calculate the mass inflow, outflow, and net rate as follows,

$$\dot{M}_{\text{in}}(r) = 4\pi r^2 \int_0^{\pi/2} \rho \min(v_r, 0) \sin(\theta) d\theta, \quad (24)$$

$$\dot{M}_{\text{out}}(r) = 4\pi r^2 \int_0^{\pi/2} \rho \max(v_r, 0) \sin(\theta) d\theta, \quad (25)$$

$$\dot{M}_{\text{net}}(r) = 4\pi r^2 \int_0^{\pi/2} \rho v_r \sin(\theta) d\theta. \quad (26)$$

The time-averaged accretion luminosity and mass outflow rate are given in columns 5 and 6 of Table 1, respectively. The last column of Table 1 gives the ratio of mass outflow rate at the outer boundary (r_{max}) to the mass accretion rate at the inner boundary (r_{min}), i.e., $\eta_w = \dot{M}_{\text{out}}(r_{\text{max}})/\dot{M}_{\text{a}}(r_{\text{min}})$.

4.1 The fiducial run

We choose model R7a from Liu et al. (2013) and compare it with its “updated” version, i.e., the fiducial model in our paper model M7. The parameters are: $M_{\text{BH}} = 10^8 M_{\odot}$, $r_* = 3r_s = 8.8 \times 10^{13}$ cm, $L_{\text{Edd}} = 1.25 \times 10^{46}$ erg s $^{-1}$, $\rho_0 = 5.0 \times 10^{-20}$ g cm $^{-3}$, and $T_0 = 2.0 \times 10^6$ K. The only difference between models M7 and R7a lies in the calculation of radiation force due to X-ray photons from the central AGN, as we state in Section 3.4.

Figure 1 shows the comparison of some model results between the two models. The top two panels show the radial profiles of the mass inflow, outflow and net rates. The bottom two panels, from left to right, show the radial profiles of gas density and temperature, respectively. They are averaged over three grids above the equatorial plane. The contours of the gas density and temperature of the two models are shown in Figure 2.

Comparing the top-left and top-right panels of Figure 1, one can see that overall in model M7 the outflow rate becomes larger compared to model R7a, and the inflow rate at the inner boundary of the simulation domain becomes smaller. In model R7a, the inflow rate decreases from the outer boundary to $6 \times 10^4 r_*$; while in model M7, the inflow rate keeps decreasing from the outer boundary to the inner

boundary. This is consistent with the fact that at small radii, the outflow rate in model M7 is larger than that in model R7a. For example, at $\sim 2 \times 10^3 r_*$ the outflow rate in model R7a is 0.2×10^{25} g s $^{-1}$, while it is 20×10^{25} g s $^{-1}$ in model M7. The result is consistent with the left column of Figure 2. In this figure, we can see that compared to model R7a, the dense outflow region can reach to a much smaller θ angle in model M7. In addition to the difference of mass flux between the two models, in model M7 the density and temperature of the gas around the equatorial plane become lower compared to model R7a.

To explain the above results, we plot the forces (normalized by gravity) in both radial and vertical directions in Figure 3. This Figure has four panels. The top two panels are for model M7. The bottom two panels are for model R7a. In the left panels we plot the sum of the radiation force due to Thomson scattering of X-ray photons from the central AGN ($F_{\text{c,x}}$) and the line force due to the UV photons from the central AGN ($F_{\text{c,o}}$). We note that the line force ($F_{\text{c,o}}$) is significantly stronger than $F_{\text{c,x}}$. In the right panels, we plot the re-radiation force in the vertical direction due to Thomson scattering (F_{re}). It is clear that the re-radiation force (F_{re}) in the vertical direction is significantly stronger than the line force ($F_{\text{c,o}}$) in the radial direction. The re-radiation force can be decomposed into two forces, one is in the radial direction ($F_{\text{re,r}}$), the other one is in the theta direction ($F_{\text{re},\theta}$). $F_{\text{re,r}}$ is significantly larger than the line force due to the UV photons from the central AGN ($F_{\text{c,o}}$). Therefore, in the present paper, the outflows are mainly driven by the re-radiation force. If the re-radiation force is not included, outflows can also be driven by the line force ($F_{\text{c,o}}$), but the mass flux of the outflow will be much smaller (see the comparison in Figure 1 of Liu et al. 2013).

From Figure 3, we can see that the re-radiation force in the vertical direction in model M7 is much stronger than that in model R7a. Therefore, in model M7, gas can be more easily pushed to high latitudes. This is the reason that in model M7 the gas density at the mid-plane is lower. The gas density in the outflow region in model M7 is higher. Thus, the outflow mass flux in model M7 is higher. Because of the stronger mass loss in outflow in model M7, the radial density profile becomes flatter, thus the compression heating becomes weaker. This is why the temperature of the gas in model M7 becomes lower (see the bottom-right panel of Figure 1 and Figure 2). From Eq. (22), we can see that in the re-radiation force, there are three terms. We have calculated the individual terms and found that the largest term is the one related to the line cooling. In model M7, the gas density in outflow region is higher and temperature is lower. Therefore, the line cooling is stronger (see Eq. 13) in model M7, which induces a stronger re-radiation force.

Additional properties of the outflow for the fiducial runs have been shown in Figure 4. In this figure, similar to the Figure 5 in Liu et al. (2013), we show the time-averaged angular and radial profiles of some outflow properties. Red and blue colours represent M7 and R7a models, respectively. The first row, from left to right, shows the angular distribution of the mass flux and density at the outer boundary of the simulation domain, i.e., ~ 6 pc. We can see that no outflow is present in the range of $\theta > 68^\circ$. Compared to model R7a, the main mass flux of the outflow in M7 occurs in a broader range of angles, $20^\circ < \theta < 68^\circ$. The time-averaged

Table 1. Summary of models with different parameters.

Run Number	Model	ρ_0 (10^{-21} g cm $^{-3}$)	T_0 (10^6 K)	L_{acc} (L_{Edd})	$\dot{M}_{\text{out}}(r_{\text{max}})$ (10^{25} g s $^{-1}$)	η_w
(1)	(2)	(3)	(4)	(5)	(6)	(7)
1	R5a	10	2	0.77(0.04)	37.95(8.71)	2.88(0.70)
2	R6a	20	2	1.19(0.16)	67.30(10.90)	3.35(0.78)
3	R7a	50	2	2.02(0.02)	139.13(5.03)	3.99(0.14)
4	R8b	100	2	3.14(0.27)	202.05(28.40)	3.75(0.59)
...
5	M5	10	2	0.79(0.1)	46.84(6.5)	3.62(1.33)
6	M6	20	2	1.01(0.02)	82.46(16.3)	4.89(0.35)
7	M7	50	2	1.64(0.08)	134.12(29.75)	4.93(0.4)
8	M8	100	2	1.97(0.46)	404.05(38.13)	12.44(1.51)
...
9	M9	10	20	1.29 (0.01)	123.14(8.65)	5.71(0.78)
10	M10	50	20	2.61(0.07)	1000.48(16.64)	23.15(3.34)

Note. Values in parentheses in Columns 5, 6 and 7 are the normalized standard deviations σ_n of the time series values.

angular profiles of density for the two models are similar. The middle-left panel shows the radial profile of the mass flux-weighted radial velocities of the outflows. We can see from the figure that the velocity increases sharply with radius in the innermost region. The velocity reaches its maximum values around $\sim 10^3 r_*$. At larger radii, the velocity decreases with increasing radius. Such a decrease is mainly due to the injection of new gas into the outflow at large radii. We note that in model M7 the decrease of velocity at large radii occurs only until $6 \times 10^4 r_*$, while in model R7a it occurs at a much smaller radius, $4 \times 10^3 r_*$. Overall, the velocity of outflow in model M7 is significantly larger than that in model R7a. This is because of the enhancement of the radiation force in model M7. The middle-right panel shows the angular distribution of outflow velocity at 6 pc. We can see a similar behaviour in two models except for a sudden drop near the polar region.

We define fluxes of momentum, kinetic energy, and thermal energy of outflow as follows,

$$\dot{p}_w(r) = 4\pi r^2 \int_0^{\pi/2} \rho v_r^2 \sin(\theta) d\theta \quad \text{for } v_r > 0, \quad (27)$$

$$\dot{E}_k(r) = 2\pi r^2 \int_0^{\pi/2} \rho v_r^3 \sin(\theta) d\theta \quad \text{for } v_r > 0, \quad (28)$$

$$\dot{E}_{\text{th}}(r) = 4\pi r^2 \int_0^{\pi/2} e v_r \sin(\theta) d\theta \quad \text{for } v_r > 0, \quad (29)$$

The solid and dotted lines in the bottom-left panel of Figure 4 show the radial profiles of these quantities in both models. In accordance with the mass flux and velocity of wind in the two models shown above, the momentum flux of wind in model M7 is much larger than that in model R7a. Also shown in the figure is the momentum flux of radiation from the AGN for comparison purpose. It can be seen that the momentum flux of radiation is higher than that of outflow at all radii. This is reasonable. In both models, the momentum flux of wind, \dot{p}_w , increases with increasing radius and gets closer to the radiation flux with the increasing radius. The percentage of the radiation momentum flux entrained by the

wind is even as high as $\sim 60\%$ for model M7. This value is much higher than that of model R7a. The reason is that, as we can see from Figure 2, the density of the gas in the wind region in model M7 is higher than that of model R7a so more radiation momentum can be captured by wind in model M7. The bottom-right panel of Figure 4 shows the kinetic (\dot{E}_k) and thermal energy fluxes (\dot{E}_{th}) of the outflow. The kinetic energy of outflow in model M7 is about 10 times higher than that in model R7a. In both models, the kinetic energy flux is much higher than the thermal energy flux so the wind motion is supersonic.

The top panel of Figure 5 shows the time evolution of AGN luminosity in unit of Eddington luminosity, $L_{\text{acc}}/L_{\text{Edd}}$ for models M7 and R7a. Column 5 in Table 1 also shows the corresponding time-averaged luminosities with the standard deviations σ_n . One problem Liu et al. 2013 hoped to solve by investigating the line-force driven wind is the so-called sub-Eddington puzzle. That is, observations show that the luminosity of almost all AGNs are sub-Eddington (Kollmeier et al. 2006; Steinhardt & Elvis 2010), while theoretically the luminosity of an accretion flow can easily be super-Eddington given the abundant gas supply in galactic center region. This puzzle is not solved in Liu et al. 2013, i.e., the wind is not strong enough to reduce the AGN accretion rate. Although the line force is increased in the present work, the luminosity in model M7 is still super-Eddington, $L_{\text{acc}}/L_{\text{Edd}} \sim 1.64$. Thus the sub-Eddington puzzle has not been solved by these modifications. One reason may be that the accretion rate should continue to decrease within the inner boundary of our simulation domain. Another reason is that in addition to radiation which we have included here, the AGN will also produce winds and these winds will also interact with the gas in our simulation domain and reduce the accretion rate (e.g., Ciotti & Ostriker 1997, 2001, 2007; Yuan et al. 2018; Bu & Yang 2019).

4.2 The effects of gas temperature and density

We study the effect of T_0 and ρ_0 in this section. The corresponding models are presented in Table 1. The bottom panel of Figure 5 shows the time evolution of the accretion

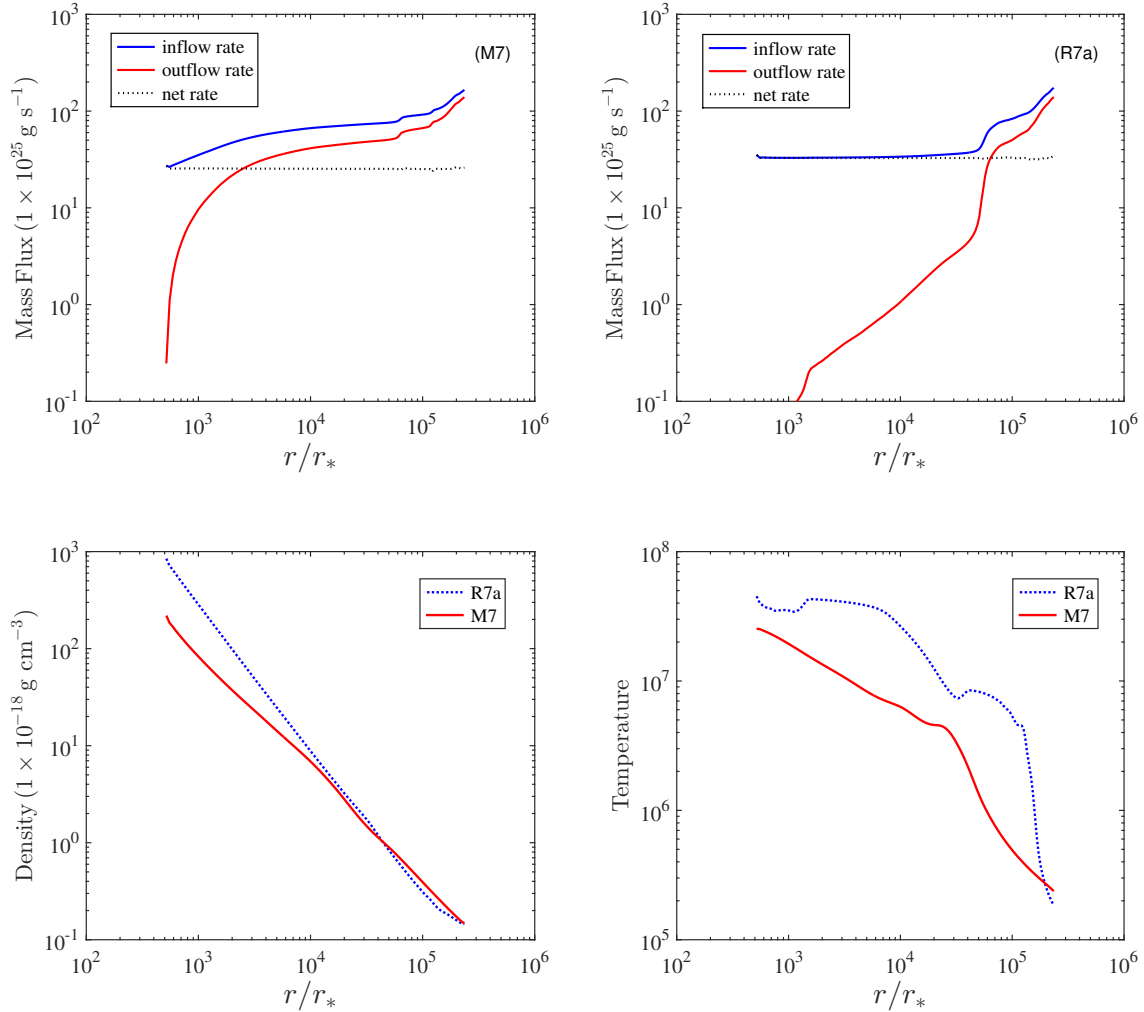


Figure 1. Comparison between models R7a and M7. The only difference between models M7 and R7a lies in the calculation of radiation force due to X-ray photons from the central AGN (see Section 3.4). Top panel: the radial profiles of mass inflow rate (blue solid lines), outflow rate (red solid lines) and the net rate (black dotted lines) in unit of 10^{25} g s^{-1} . Bottom panel: the radial profiles of gas density (left panel, in unit of $10^{-18} \text{ g cm}^{-3}$) and temperature (right panel, in unit of K) averaged over three grids above the equatorial plane. The data are time-averaged.

luminosity for models M5 (green line), M7 (red line), M9 (blue line), and M10 (black line). Figure 6 shows the snapshots of contours of gas density and temperature of models M5, M9 and M10.

From Figure 5, we see that with the increase of ρ_0 , the accretion luminosity increases. This is not surprising. What is interesting is the effect of T_0 . From model M5 to M9 and from M7 to M10, the only change is the increase of T_0 . We can see from Figure 5 that the increase of T_0 has two effects. One is the increase of luminosity; another one is that the light curve becomes very smooth. These two effects are related with each other, as we explain below. To explain such effects, the key point is that the value of the line force is a function of gas temperature (see Proga et al. 2000 for details). When T_0 increases from $2 \times 10^6 \text{ K}$ to $2 \times 10^7 \text{ K}$, the

line force significantly decreases. Consequently, as we can see from Figure 6, the inflow region becomes much wider, from $\theta \sim 60^\circ - 90^\circ$ in model M5 to $\theta \sim 30^\circ - 90^\circ$ in model M9. This explains why the accretion rate and subsequently the luminosity increases. In model M9, when the accreting gas reaches the innermost region, its density becomes very large and temperature significantly decreases because of the strong radiative cooling. Radiative line force then begins to play its role and produce an outflow. This is the origin of the high-density filament-like outflowing structure seen in model M9 at $\theta \sim 30^\circ$.

In model M5, the temperature in all θ region is not high so the line force can play its role in all these region. Consequently, when luminosity becomes strong the line force also becomes strong; thus accretion can be suppressed and lumi-

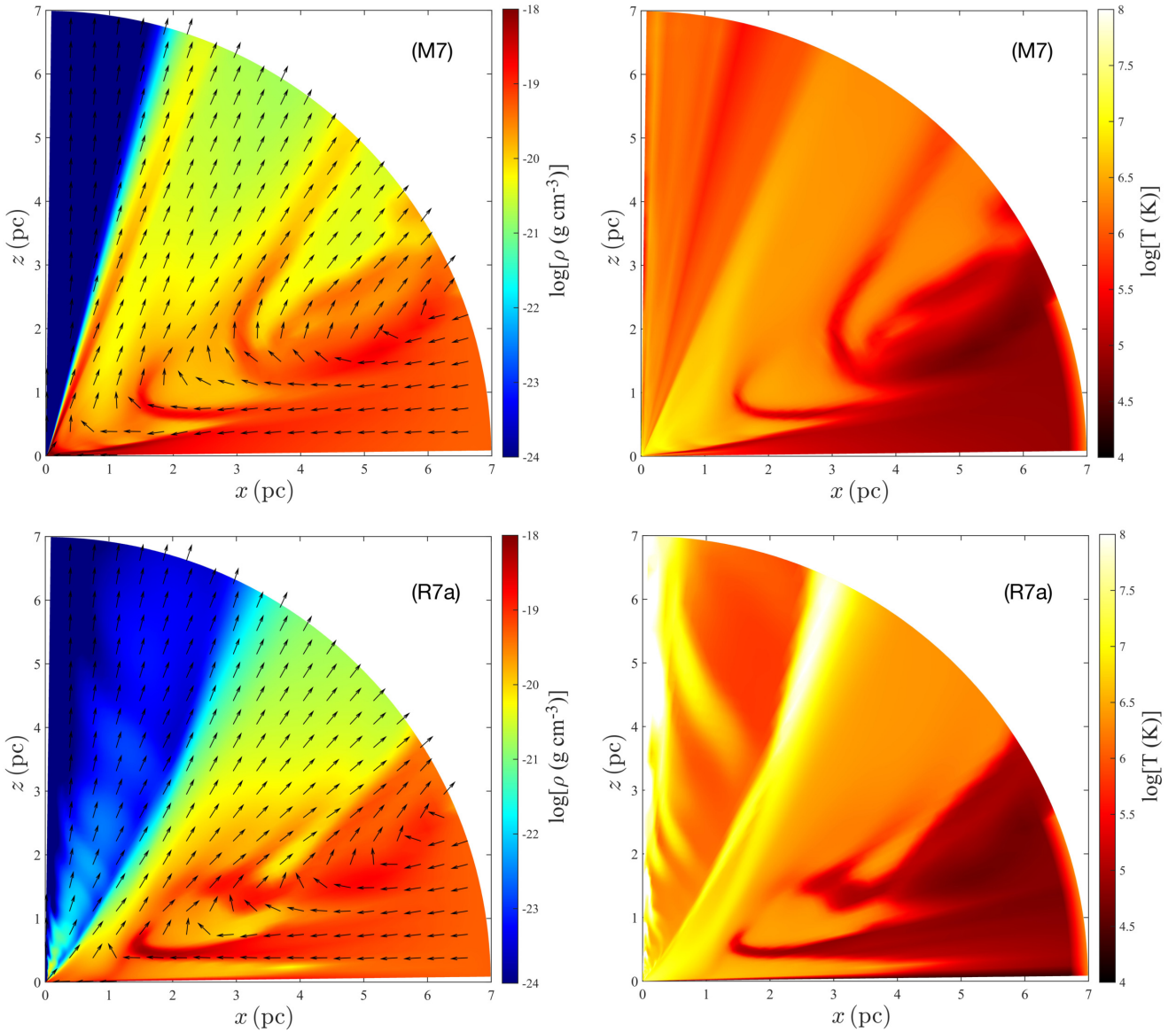


Figure 2. Snapshots of contours of logarithmic gas density (left column) and logarithmic temperature (right column) at the steady state.

nosity decreases. This results in a weaker line force and subsequently stronger accretion and luminosity. This explains why we see strong fluctuation in the light curve of model M5. Compared to model M5, in model M9, the difference of temperature of inflow and outflow is significant and the two regions are spatially well separated. The temperature in the inflow region is always high, while the temperature in the outflow region is always low. So there is almost no fluctuation in this model and the light curve is smooth.

4.3 Observational implications

Outflow is widely observed in different kinds of AGNs, usually in the form of blue-shifted absorption lines (BAL) (e.g., Crenshaw et al. 2003; Tombesi et al. 2010, 2012a,b; Kaastra et al. 2012; Gofford et al. 2015; He et al. 2019). In Gofford et

al. 2015, they performed a systematic analysis to the outflow properties in a sample of 51 *Sukaku*-observed AGNs. They found that the properties of wind cover a large range. Typically they are detected at distance from $\sim 0.001 - 1$ pc, the outflow velocity is in the range between $0.01 - 0.1c$, the mass outflow rate falls between $10^{24} - 10^{26} \text{ g s}^{-1}$, and the kinetic luminosity of wind ranges between $10^{43} - 10^{45} \text{ erg s}^{-1}$.

We now examine whether the observed wind properties are consistent with our theoretical predictions. We choose M5 since its corresponding accretion luminosity is $79\% L_{\text{Edd}}$, which is close to the typical luminosity of a luminous AGN as sampled in Gofford et al. 2015. We find that the typical outflow velocity is $0.02c$, the outflow mass flux becomes significant from 0.07pc , the maximum mass outflow rate achieved at the outer boundary is $\sim 4.7 \times 10^{26} \text{ g s}^{-1}$ (Table 1), and the kinetic luminosity of outflow is $\sim 3 \times 10^{43} \text{ erg s}^{-1}$. All

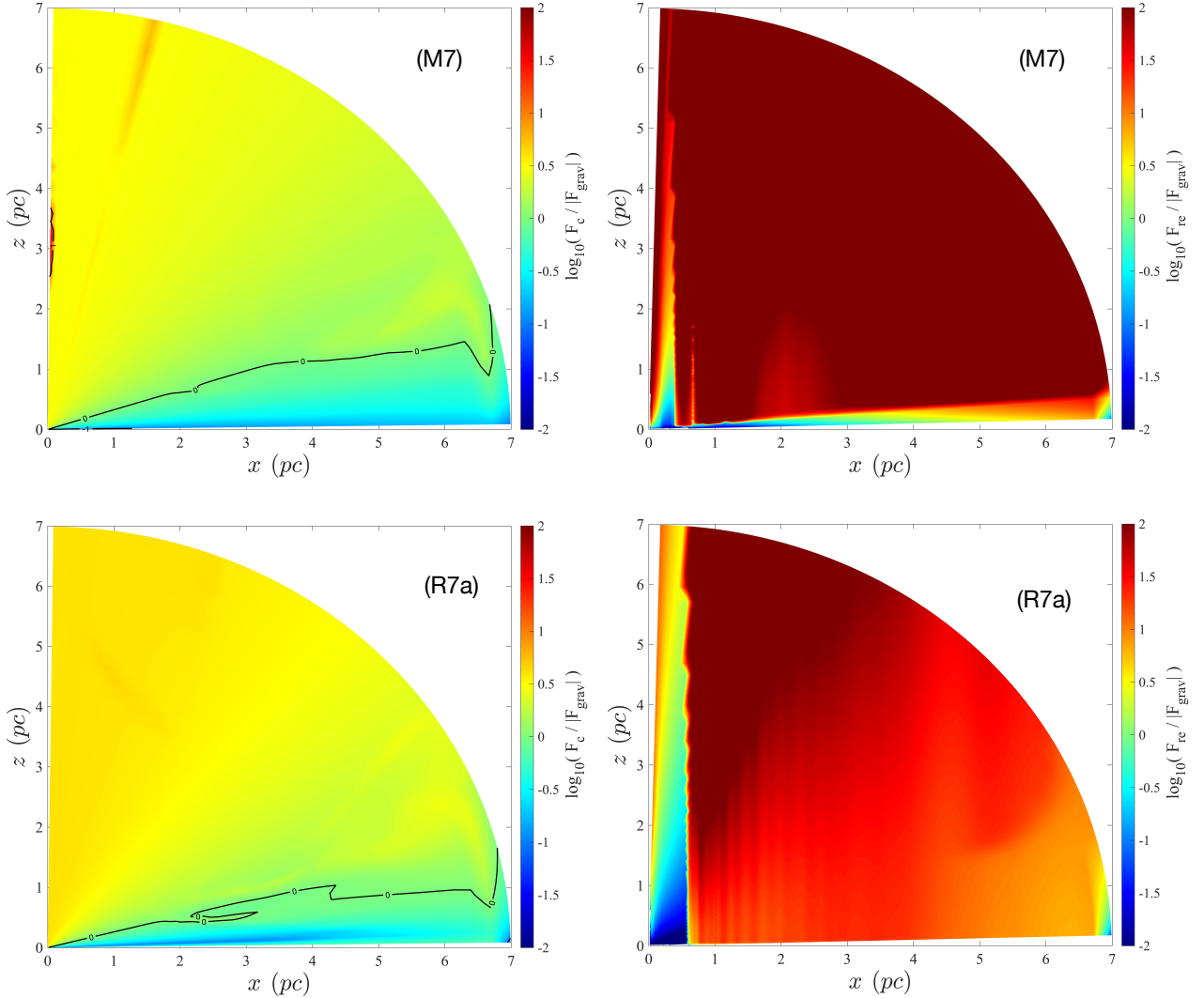


Figure 3. Comparison between total forces in radial (F_c) and vertical (F_{re}) directions for models R7a and M7. The forces are in units of the BH Newtonian gravity ($F_{grav} = GM/r^2$). The left panels represent the sum of the radiation force due to Thomson scattering of X-ray photons from the central AGN ($F_{c,x}$) and the line force due to the UV photons from the central AGN ($F_{c,o}$). The right panels show the re-radiation force in vertical direction due to Thomson scattering (F_{re}). The lines in the left column show the location where $\log_{10}(F_c/|F_{grav}|) = 0$.

these values are roughly in the observed range of outflow properties.

As we explained in subsection 4.1, the outflow found in this paper is driven by both the line force and re-radiation force. The properties of the outflows are consistent with observations (Gofford et al. 2015). Therefore, the BAL winds in AGNs may be driven by the combination of line and re-radiation forces. As mentioned above, if re-radiation force is neglected, outflow can be driven by line force. However, in this case, the mass flux of outflow is lower. Therefore, we cannot eliminate the possibility that the observed BAL outflow is driven by line force. We can then conclude that with the help of re-radiation force, the BAL outflow can be stronger.

5 SUMMARY AND DISCUSSION

In this paper, we have investigated the dynamics of accretion flow with the irradiation from the central AGN by performing two-dimensional hydrodynamical simulations. We focus on relatively large radii, with the simulation domain ranging from 0.01 – 7 pc. The mass of the central black hole is $M_{BH} = 10^8 M_\odot$. The central engine has two components, i.e., a standard thin disc and a spherical hot corona, which emits optical/UV and X-ray radiation. Both the optical/UV and X-ray photons can produce a radiation force by Thomson scattering. Moreover, the optical/UV photons can also produce a line force, since the gas is not fully ionized thus the interaction cross-section is significantly amplified compared to the pure Thomson scattering. The main improvement in our present work compared to our previous one (i.e., Liu et al. 2013) is that we now correctly include the radiation

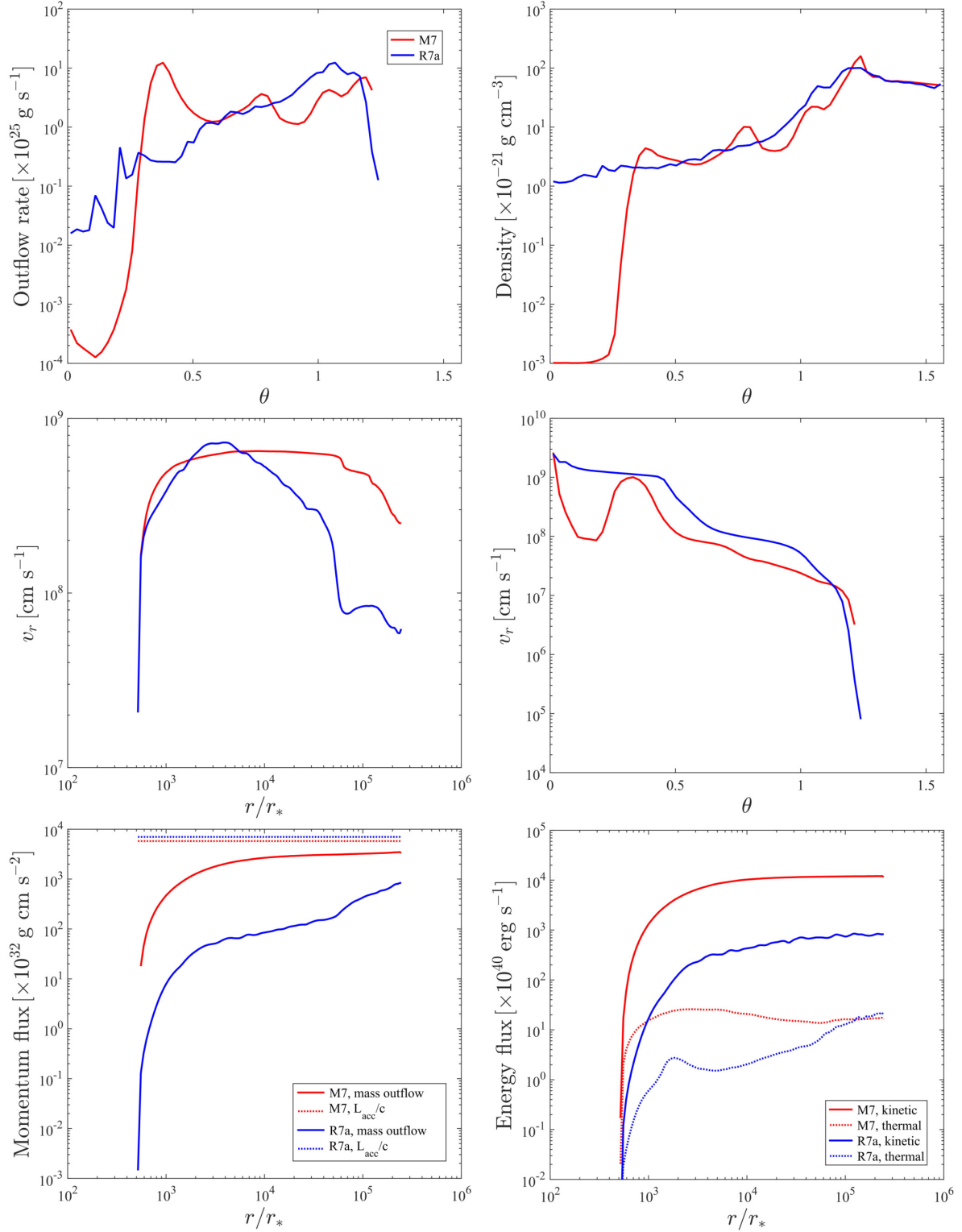


Figure 4. Properties of outflow in models M7 (red lines) and R7a (blue lines). Top: the angular distribution of the mass outflow rate (top-left panel, in unit of 10^{25} g s^{-1} ; defined as $\dot{M}_{\text{out}}(\theta) = 2\pi r^2 \rho \max(v_r, 0) \sin(\theta) \Delta\theta$) and density (top-right panel, in unit of $10^{-21} \text{ g s}^{-1}$ at the outer boundary of the simulation domain; Middle: the radial profile of the mass flux-weighted radial velocity of the outflow (left panel, in unit of cm s^{-1}) and angular distribution of the outflow velocity (right panel, in unit of cm s^{-1}); Bottom-left: the radial profile of the momentum flux of the outflow (in unit of $10^{32} \text{ g cm s}^{-2}$; solid lines) and radiation flux from the central AGN (L_{acc}/c ; dotted lines). Bottom-right: the radial profile of the kinetic (the solid lines) and the thermal (dotted lines) energy fluxes in unit of $10^{40} \text{ erg s}^{-1}$. All the lines in this figure are time-averaged.

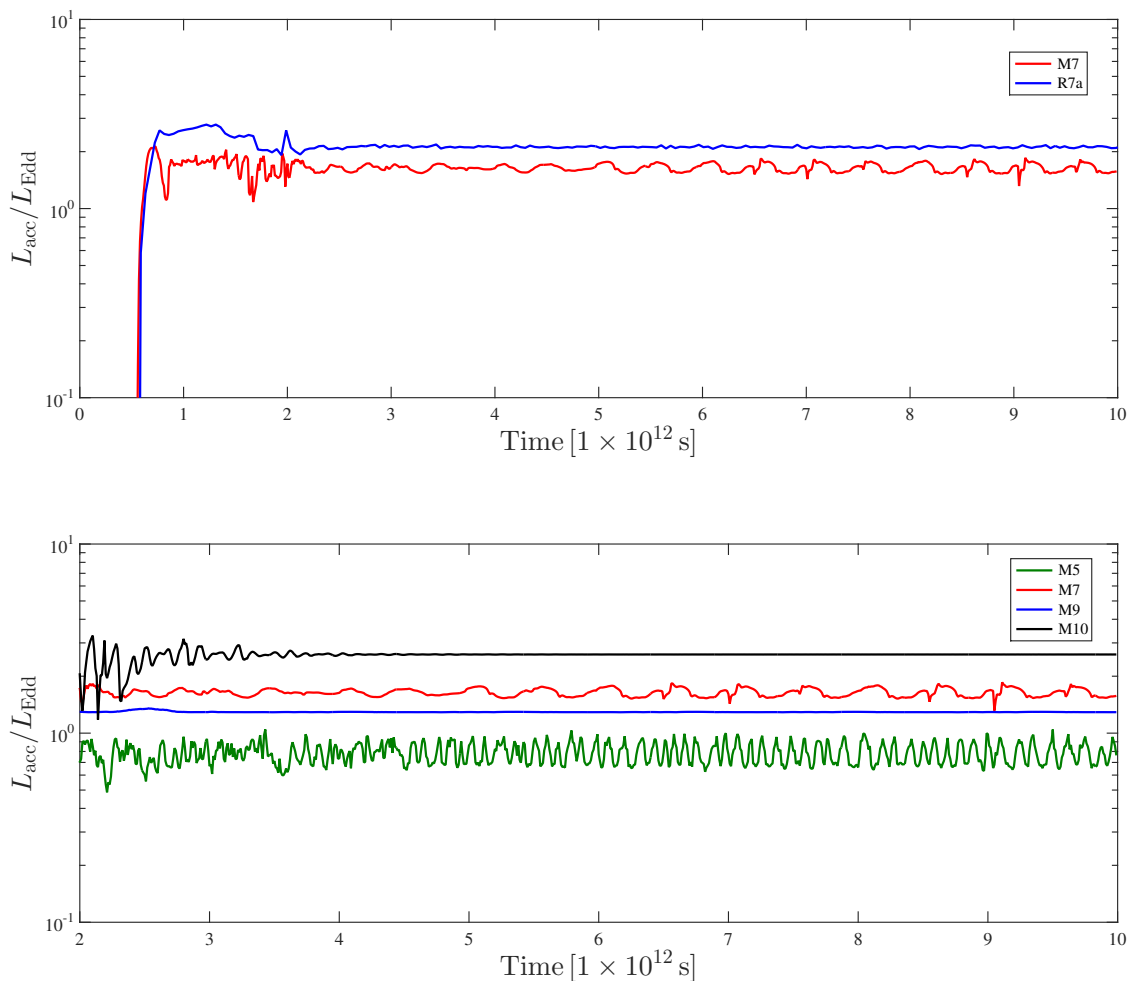


Figure 5. Time evolution of the AGN luminosity in unit of Eddington luminosity L_{Edd} for different models. Top panel: comparison between models R7a and M7. Bottom panel: The green, red, blue and black lines correspond to models M5, M7, M9 and M10, respectively.

force corresponding to the Thomson scattering by the X-ray photons (equation 21 in section 3.4).

Taking a fiducial model M7 as an example, we find that such an update of the radiation force results in an enhancement of the mass outflow flux compared to the previous corresponding model (i.e., model R7a in Liu et al. 2013) (Fig. 1). We have calculated the total forces in the radial and vertical directions in Fig. 3. we find that the re-radiation force in vertical direction in model M7 is much stronger than that in model R7a. Correspondingly, the mass inflow rate decreases, and the temperature and density of the gas around the equatorial plane also change somewhat (Fig. 1). The typical velocity of outflow also increases in model M7 in most region by a factor of a few (middle panel of Fig. 4). Because of the increase of mass outflow rate and velocity, the momentum flux and kinetic flux of outflow increases roughly by a factor of 10 (bottom panel of Fig. 4). For model M7, the momentum flux of outflow is as high as 60% of the

momentum flux of radiation. This percentage is significantly higher than model R7a. This is because the density of outflow in model M7 is higher thus can entrain the momentum of more photons.

We have also examined the effects of density and temperature of the gas in the initial state of our simulations, ρ_0 and T_0 . We find that the effect of T_0 is interesting. When T_0 becomes higher, the inflow rate increases (Fig. 5). This is because the line force becomes weaker due to the increase of T_0 thus accretion becomes stronger. Moreover, when this gas is accreted into the innermost region, the density becomes high and thus temperature decreases (Fig. 6) so the line force becomes strong; a strong outflow will be produced there. Such an outflow has a filamentary-like structure (Fig. 6) and the outflow region is well separated from the inflow region. This results in a smooth light curve of the accretion luminosity, rather than the fluctuated light curve when T_0 is lower (bottom of Fig. 5).

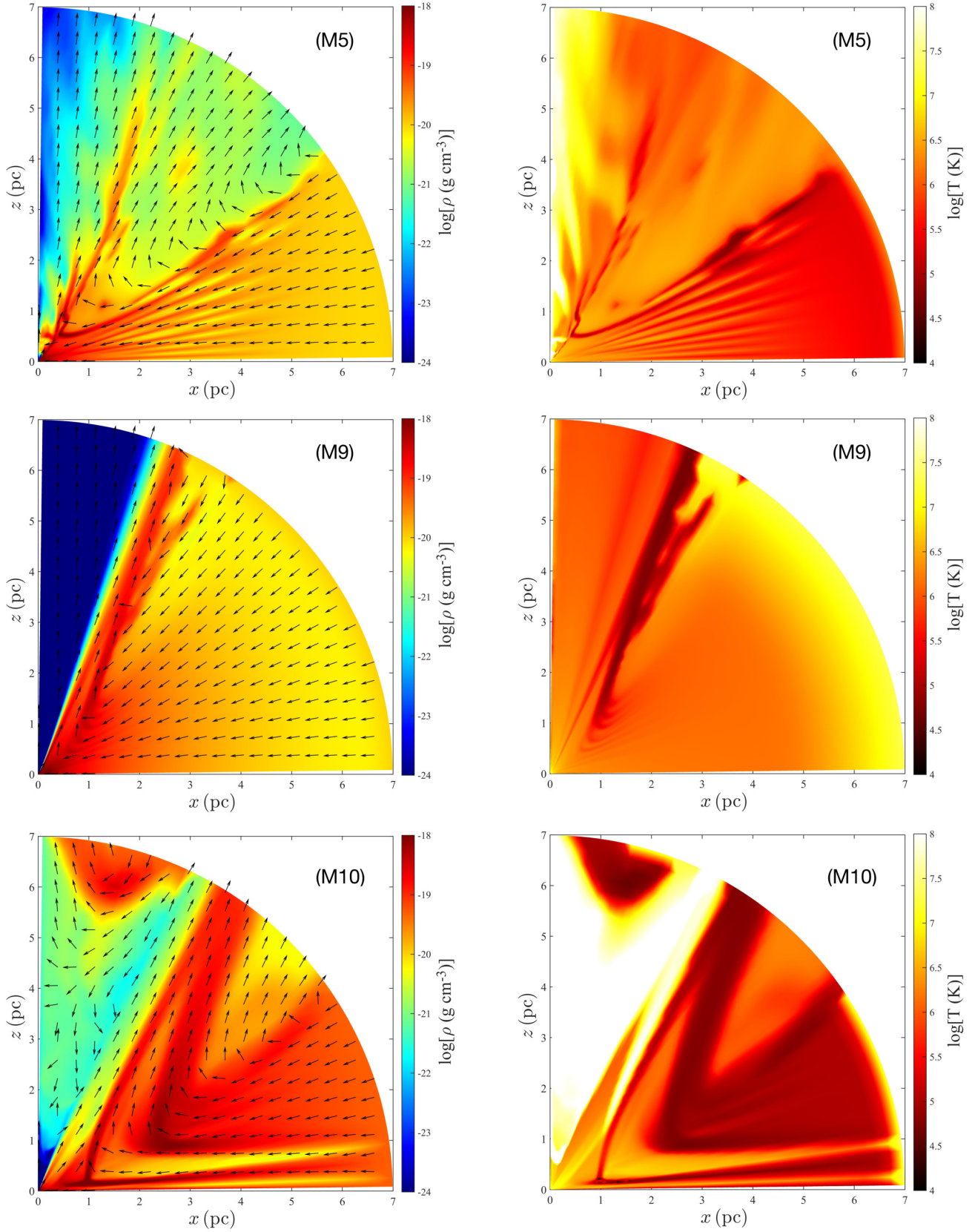


Figure 6. Snapshots of contours of logarithmic gas density (left-hand column) and logarithmic temperature (right-hand column) correspond to models M5, M9 and M10, respectively. The density over-plotted with the directions of poloidal velocity as arrows (left column). The figures are placed in order of increasing density and temprutere at $r = r_{\text{max}}$ (see Table 1).

We have also compared the properties of outflow obtained in our simulations with those outflow obtained from blue-shifted absorption line observations (Gofford et al. 2015). These properties include the mass outflow rate, velocity, and kinetic luminosity at a given distance from the central black hole. While the observed range is large, we find that our simulation results are well within the observed range. Thus the combination of radiation line-force and re-radiation force we have studied in this work could be a candidate mechanism for the widely observed outflow in AGNs.

There are several caveats in this study. One is that our approach for calculating the radiation and re-radiation forces is rather simple. In principle, the full radiation transfer calculation is desirable. Simulations with radiative transfer are expensive but more realistic. Another caveat here is that, we do not include the interaction of radiation with dust. The photon-dust interaction can enhance the mass flux of outflow. In the present work, we only consider the low-angular momentum case. Next step, we will consider the case of a large-angular momentum. In this case, a rotationally supported disc will be formed and the dynamics of accretion flow may change. Another important case one may consider is the effect of magnetic field. Usually the inclusion of magnetic field will enhance the outflow significantly. It will be interesting to study outflow by combining the radiation and magnetic field.

ACKNOWLEDGEMENTS

Amin Mosallanezhad is supported by the Chinese Academy of Sciences President's International Fellowship Initiative, (PIFI), Grant No. 2018PM0046. D.-F.B. is supported in part by the Natural Science Foundation of China (grant 11773053). This work is supported in part by the National Key Research and Development Program of China (Grant No. 2016YFA0400704), the Natural Science Foundation of China (grants 11573051, 11633006, 11650110427, 11661161012, U1431228, 11233003, and 11421303), the Key Research Program of Frontier Sciences of CAS (No. QYZDJSSW-SYS008), and the Astronomical Big Data Joint Research Center co-founded by the National Astronomical Observatories, Chinese Academy of Sciences and the Alibaba Cloud. The computation has made use of the High Performance Computing Resource in the Core Facility for Advanced Research Computing at Shanghai Astronomical Observatory.

REFERENCES

- Abramowicz, M. A., Czerny, B., Lasota, J. P., & Szuszkiewicz, E. 1988, *ApJ*, 332, 646
- Blandford, R. D., & Begelman, M. C. 1999, *MNRAS*, 303, L1
- Blondin J. M., 1994, *ApJ*, 435, 756
- Bu, D.-F., Yuan, F., Gan, Z.-M., & Yang, X.-H. 2016, *ApJ*, 823, 90
- Bu, D.-F., Yang, X.H. 2019, *ApJ*, 871, 138
- Castor J. I., Abbott D. C., Klein R. I., 1975, *ApJ*, 195, 157
- Cheung, E., Bundy, K., Cappellari, M., et al. 2016, *Nature*, 533, 504
- Ciotti, L., & Ostriker, J. P. 1997, *ApJL*, 487, L105
- Ciotti, L., & Ostriker, J. P. 2001, *ApJ*, 551, 131
- Ciotti, L., & Ostriker, J. P. 2007, *ApJ*, 665, 1038
- Clarke D. A., 1996, *ApJ*, 457, 291
- Crenshaw, D. M., Kraemer, S. B., & George, 2003, *ARA&A*, 41, 117
- Fabian, A. C. 2012, *ARA&A*, 50, 455
- Ferrarese, L., & Merritt, D. 2000, *ApJL*, 539, L9
- Fukue J., 2000, *PASJ*, 52, 829
- Gültekin, K., Richstone, D. O., Gebhardt, K., et al. 2009, *ApJ*, 698, 198
- Gan, Z., Yuan, F., Ostriker, J. P., Ciotti, L., & Novak, G. S. 2014, *ApJ*, 789, 150
- Gan, Z., Ciotti, L., Ostriker, J. P., & Yuan, F. 2019, *ApJ*, 872, 167
- Gebhardt, K., Bender, R., Bower, G., et al. 2000, *ApJL*, 539, L13
- Gofford, J., et al. 2015, *MNRAS*, 451, 4169
- Graham, A. W., Onken, C. A., Athanassoula, E., & Combes, F. 2011, *MNRAS*, 412, 2211
- Hagino K., Odaka H., Done C., Gandhi P., Watanabe S., Sako M., Takahashi T., 2015, *MNRAS*, 446, 663
- Häring, N., & Rix, H.-W. 2004, *ApJL*, 604, L89
- Hardee P. E., Clarke D. A., 1992, *ApJ*, 400, L9
- Hayes J. C., Norman M. L., Fiedler R. A., Bordner J. O., Li P. S., Clark S. E., ud-Doula A., Mac Low M.-M., 2006, *ApJS*, 165, 188
- He, Z. et al. 2019, *Nature Astronomy*, 3, 265
- Homan, J., Neilsen, J., Allen, J. L., et al. 2016, *ApJL*, 830, L5
- Kaasra J. S. et al., 2012, *A&A*, 539, A117
- Kormendy, J., & Ho, L. C. 2013, *ARA&A*, 51, 511
- Kormendy, J., & Richstone, D. 1995, *ARA&A*, 33, 581
- Kollmeier J. et al., 2006, *ApJ*, 648, 128
- Kurosawa R., Proga D., 2008, *ApJ*, 674, 97
- Kurosawa R., Proga D., 2009, *MNRAS*, 397, 1791 (KP09)
- Li, J., Ostriker, J., & Sunyaev, R. 2013, *ApJ*, 767, 105
- Li, Y. P., Yuan, F., Mo, H. J., et al. 2018, *ApJ*, 866, 70
- Liu, C., Yuan, F., Ostriker, J. P., Gan, Z., & Yang, X. 2013, *MNRAS*, 434, 1721
- Ma, R.-Y., Roberts, S. R., Li, Y.-P., & Wang, Q. D. 2019, *MNRAS*, 483, 5614
- Magorrian, J., Tremaine, S., Richstone, D., et al. 1998, *AJ*, 115, 2285
- Marconi, A., & Hunt, L. K. 2003, *ApJL*, 589, L21
- Mosallanezhad, A., Bu, D., & Yuan, F. 2016, *MNRAS*, 456, 2877
- Narayan, R., Sadowski, A., Penna, R. F., & Kulkarni, A. K. 2012, *MNRAS*, 426, 3241
- Ohsuga, K., Mori, M., Nakamoto, T., & Mineshige, S. 2005, *ApJ*, 628, 368
- Ostriker J. P., Choi E., Ciotti L., Novak G. S., Proga D., 2010, *ApJ*, 722, 642
- Paczynski, B., & Wiita, P. J. 1980, *A&A*, 88, 23
- Proga D., Stone J. M., Kallman T. R., 2000, *ApJ*, 543, 686
- Proga D., 2007a, *ApJ*, 661, 693
- Proga, D., Ostriker, J. P., & Kurosawa, R. 2008, *ApJ*, 676, 101
- Sazonov S. Y., Ostriker J. P., Ciotti L., Sunyaev R. A., 2005, *MNRAS*, 358, 168
- Sazonov S. Y., Ostriker J. P., Sunyaev R. A., 2004, *MNRAS*, 347, 144
- Shakura N. I., Sunyaev R. A., 1973, *A&A*, 24, 337
- Steinhardt C. L., & Elvis M., 2010, *MNRAS*, 402, 2637
- Stevens I. R., Kallman T. R., 1990, *ApJ*, 365, 321
- Stone J. M., Norman M. L., 1992, *ApJS*, 80, 753
- Tombesi, F., Cappi, M., Reeves, J. N., Palumbo, G. G. C., Yaqoob, T., Braito, V., & Dadina, M. 2010, *A&A*, 521, A57
- Tombesi, F., Cappi, M., Reeves, J. N., & Braito, V. 2012a, *MNRAS*, 422, L1
- Tombesi, F., Sambruna, R. M., Marscher, A. P., Jorstad, S. G., Reynolds, C. S., & Markowitz, A. 2012b, *MNRAS*, 424, 754
- Tombesi, F., Tazaki, F., Mushotzky, R. F., et al. 2014, *MNRAS*, 443, 2154

- Tremaine, S., Gebhardt, K., Bender, R., et al. 2002, ApJ, 574, 740
- Wang, Q. D., Nowak, M. A., Markoff, S. B., et al. 2013, Science, 341, 981
- Weinberger, R., Springel, V., Hernquist, L., et al. 2017a, MNRAS, 465, 3291
- Yang, X., Yuan, F., Ohsuga, K., & Bu, D. 2014, ApJ, 780, 79
- Yoon, D., Yuan, F., Gan, Z. M., et al. 2018, ApJ, 864, 6
- Yuan, F., Wu, M. & Bu, D. 2012a, ApJ, 761, 129
- Yuan, F., Bu, D., & Wu, M. 2012b, ApJ, 761, 130
- Yuan, F., Gan, Z., Narayan, R., et al. 2015, ApJ, 804, 101
- Yuan, F., Ostriker, J. P., Yoon, D, Li, Y. P., Ciotti, L., Gan, Z., Ho, L. C., Guo, F. 2018, ApJ, 857, 121